

COLOR AFFINE SUBSPACE PURSUIT FOR COLOR ARTIFACT REMOVAL

Kazuki Yamanaka¹, Seisuke Kyochi¹, Shunsuke Ono², and Keiichiro Shirai³

1: The University of Kitakyushu, Fukuoka, Japan

2: Tokyo Institute of Technology, Tokyo, Japan

3: Shinshu University, Nagano, Japan

Email: s-kyochi@kitakyu-u.ac.jp

ABSTRACT

This paper proposes color affine subspace pursuit (CASSP) for color artifact removal. Local patches in natural color images tend to exhibit a line distribution, so-called a *color line*. According to this characteristic, a convex-optimization-based image recovery with a local color nuclear norm (LCNN) has conventionally been introduced to promote the color line property of local patches and succeeded in removing color artifacts. It is, however, often the case that a local patch does not form a line distribution, but a union of affine subspaces (UoAS), e.g., a patch consisting of two different colors. In such regions, the LCNN often results in color fading or color smearing. This paper promotes the UoAS property, i.e., the color line or plane distribution for each affine subspace in local patches by using CASSP. Our cost function for the CASSP consists of the LCNN for each centered color distribution cluster. Experimental results show that the CASSP improves both numerical reconstruction error and subjective visual quality, compared with the LCNN.

Index Terms— Convex optimization, image recovery, color line property, local color nuclear norm, union of affine subspace

1. INTRODUCTION

Image recovery via convex optimization enables us to take a unified approach for various image processing tasks, e.g., denoising, deblurring, missing pixel recovery, super resolution, and so on [1–4]. Mathematically, for an N sample observed (vectorized) color image $\mathbf{y} \in \mathbb{R}^{3N}$ and a matrix representing a degradation process $\Phi \in \mathbb{R}^{3N \times 3N}$ (for mathematical expressions, see *Notations* in the end of this section), a desired latent image is estimated by finding a minimizer of the following cost function $\mathcal{J}(\mathbf{x})$:

$$\mathbf{x}^* = \arg \min_{\mathbf{x} \in \mathbb{R}^{3N}} \mathcal{J}(\mathbf{x}) = \arg \min_{\mathbf{x} \in \mathbb{R}^{3N}} F_{\mathbf{y}}(\Phi \mathbf{x}) + \lambda \mathcal{R}(\mathbf{x}), \quad (1)$$

where $F_{\mathbf{y}} : \mathbb{R}^{3N} \rightarrow \mathbb{R}_+$ is some data fidelity function, e.g., $F_{\mathbf{y}}(\mathbf{x}) = \frac{1}{2} \|\Phi \mathbf{x} - \mathbf{y}\|_2^2$ and $\lambda \in \mathbb{R}_+$ is a weighting coefficient. Here, to obtain high quality restored images in each task, we should design a suitable convex prior $\mathcal{R} : \mathbb{R}^{3N} \rightarrow \mathbb{R}_+$ which mathematically characterizes desired properties of ideal images, such as smoothness, patterns, and sparsity in some transformed domain. For example, total variation [5–9] and total generalized variation [10] have been proposed for smooth regions, and sparse representation by (local/non-local) frame/dictionary [11, 12], and structure-tensor total variation [13–15] for textures.

This work was supported in part by JSPS Grants-in-Aid (16H04362, 17K12710, and 17K14683) and JST-PRESTO.

In color image recovery, we often face with color artifacts, e.g., false colors in resulting estimated images, even though the state-of-the-art regularizers, which use local/non-local similarity, dictionary learning and so on, are introduced into a cost function. For example, one can observe color smearing artifacts in [16] (Fig. 8), [17] (Fig. 11), and [14] (Fig. 3). To remove color artifacts, a local color nuclear norm (LCNN) has been proposed [18, 19]. Clean color images mainly consist of local patches of which distribution is (almost) a line as shown in the regions (b) and (c) in the image *Parrots* in Fig. 1. With this property in mind, the LCNN evaluates the sum of singular values of a color matrices. Each matrix aligns R, G, and B channels of the corresponding local patch. When its cost function with the LCNN for image recovery is minimized, the color line property is promoted, and thus color artifacts are reduced.

However, it is often the case that the color line property fails in many local patches as shown in the regions (a) and (d) in Fig. 1. Such regions typically consist of two or more colors. This can be regarded as the union of affine subspaces (UoAS), i.e., lines and planes that do not necessarily go through the origin point. Since the regularization by the LCNN acts as an approximation of the color distribution toward a single low dimensional subspace, in the case of the UoAS, the LCNN causes color artifacts, e.g., color fading or color smearing across object boundaries.

This paper attempts to overcome the problem of the LCNN. First, we formulate an optimization problem that regards to promote the color affine subspace property for UoAS patches. This strategy is termed as color affine subspace pursuit (CASSP). The initial cost function of the CASSP involves a matrix factorization that makes it highly ill-posed and non-convex. Thus, to simply find an approximated solution, we modify the conventional LCNN to a centered-cluster-wise LCNN, which is based on image pre-recovery and K -means clustering, for CASSP.

The rest of this paper is organized as follows. Section 2 reviews LCNN and a primal-dual splitting (PDS) [20–23], which is a solver of a class of convex optimization used in this paper. Then, CASSP is explained in Section 3. The proposed method is evaluated in the experiments of compressed image sensing in Section 4. Finally, this paper is concluded in Section 5.

Notations: Bold-faced lower-case and upper-case letters denote vectors and matrices, respectively. Sets \mathbb{R} and \mathbb{R}_+ respectively denote real and non-negative real numbers, respectively. Real-valued and non-negative real-valued matrices of size N_r [row] and N_c [column] are described as $\mathbb{R}^{N_r \times N_c}$ and $\mathbb{R}_+^{N_r \times N_c}$. $\text{diag}(a_0, \dots, a_{M-1})$ denotes diagonal matrices. $\|\cdot\|_2$ is ℓ_2 norm. $\mathbf{I}_N \in \mathbb{R}^{N \times N}$ and $\mathbf{1}$ are reserved for the identity matrix and the all-ones vector. \otimes is the Kronecker product.

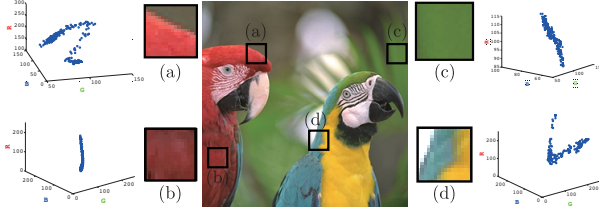


Fig. 1: Parrots and four local color distributions (patch size: 16×16) depicted in the 3 dimensional space, where each axis corresponds to R, G, and B.

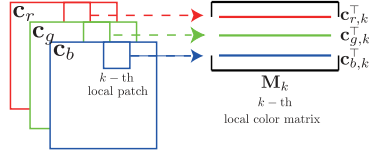


Fig. 2: Local color matrix

2. PRELIMINARIES

2.1. Local Color Nuclear Norm

The LCNN [18, 19] was proposed to promote the color line property of local patches as follows. Let an N sample color image be $\mathbf{c} = [\mathbf{c}_r^\top \mathbf{c}_g^\top \mathbf{c}_b^\top]^\top \in \mathbb{R}^{3N}$ ($\mathbf{c}_r, \mathbf{c}_g, \mathbf{c}_b \in \mathbb{R}^N$ are the R, G, and B channels, respectively). The set of indices of the pixels is $\mathcal{N} = \{1, \dots, N\}$, that of the pixels in the k -th patch ($k = 1, \dots, K$) is denoted as $\mathcal{I}_k \subset \mathcal{N}$ (patches can overlap each other), the number of its elements is $|\mathcal{I}_k|$, and all the sets of indices is $\tilde{\mathcal{I}} := \{\mathcal{I}_k\}_{k=1}^K$. Let the R, G, and B channels in the k -th patch of an input image be $\mathbf{c}_{r,k}, \mathbf{c}_{g,k}, \mathbf{c}_{b,k} \in \mathbb{R}^{|\mathcal{I}_k|}$ the color matrix corresponding to the ℓ -th patch is determined as $\mathbf{M}_k := [\mathbf{c}_{r,k} \mathbf{c}_{g,k} \mathbf{c}_{b,k}]^\top \in \mathbb{R}^{3 \times |\mathcal{I}_k|}$ (see Fig. 2). Then, the LCNN $\|\cdot\|_{\text{LC}^*}^{\tilde{\mathcal{I}}, \mathbf{w}, \boldsymbol{\mu}} : \mathbb{R}^{3\tilde{N}} \rightarrow \mathbb{R}_+$ ($\tilde{N} = \sum_{k=1}^K |\mathcal{I}_k|$) is defined as

$$\|\mathbf{x}\|_{\text{LC}^*}^{\tilde{\mathcal{I}}, \mathbf{w}, \boldsymbol{\mu}} := \sum_{k=1}^K \mu_k \|\mathbf{M}_k\|_{*, \mathbf{w}}, \quad (2)$$

where, for $\mathbf{X} \in \mathbb{R}^{p \times q}$, $\|\mathbf{X}\|_{*, \mathbf{w}} = \sum_{i=1}^r w_i \sigma_i(\mathbf{X})$ ($r = \min\{p, q\}$) is a weighted nuclear norm (NN) with some weighting coefficients¹ $\mathbf{w} = [w_1 \ w_2 \ w_3]^\top \in \mathbb{R}_+^3$. $\sigma_i(\mathbf{X})$ is the i -th largest singular value of \mathbf{X} . $\boldsymbol{\mu} := [\mu_1 \ \dots \ \mu_K]^\top \in \mathbb{R}_+^K$ relatively controls how much the color line property should be promoted for each local patch.

In finding a solution of the convex optimization problem with LCNN by some proximal splitting method, one requires the (pseudo) proximity operator of the LCNN. In general, the proximity operator of $f \in \Gamma_0(\mathbb{R}^p)^2$ is defined as [24]:

$$\text{prox}_{\gamma f} : \mathbb{R}^p \rightarrow \mathbb{R}^p : \mathbf{x} \mapsto \arg \min_{\mathbf{z} \in \mathbb{R}^p} f(\mathbf{z}) + \frac{1}{2\gamma} \|\mathbf{y} - \mathbf{x}\|_2^2. \quad (3)$$

Since patches would have overlap ($\mathcal{I}_{k_1} \cap \mathcal{I}_{k_2} \neq \emptyset$) that prevents from computing the proximity operator directly, an equivalent expression

¹In this paper, we assume that $w_1 \leq w_2 \leq w_3$ and all the nonzero singular values of each color matrix are distinct [15].

² $\Gamma_0(\mathbb{R}^p)$ is the set of proper lower semi-continuous convex functions [24] on \mathbb{R}^p .

of the LCNN, which is termed as an augmented LCNN in [18, 19], was presented. Let $\boldsymbol{\Omega}_{\tilde{\mathcal{I}}} = [\boldsymbol{\Omega}_1^\top \ \dots \ \boldsymbol{\Omega}_K^\top]^\top \in \mathbb{R}^{3\tilde{N} \times 3N}$ be an extending operator, where $\boldsymbol{\Omega}_k \in \mathbb{R}^{|\mathcal{I}_k| \times 3N}$ picks samples in the k -th local patch, i.e., $\boldsymbol{\Omega}_k \mathbf{c} = [\mathbf{c}_{r,k}^\top \ \mathbf{c}_{g,k}^\top \ \mathbf{c}_{b,k}^\top]^\top$. Then, the augmented LCNN is defined as:

$$\|\cdot\|_{\text{ALC}^*}^{\tilde{\mathcal{I}}, \mathbf{w}, \boldsymbol{\mu}} : \mathbb{R}^{3\tilde{N}} \rightarrow \mathbb{R}_+ : \mathbf{x} \mapsto \sum_{k=1}^K \mu_k \|\mathbf{M}_k\|_{*, \mathbf{w}}, \quad (4)$$

and LCNN can be represented as:

$$\|\mathbf{c}\|_{\text{LC}^*}^{\tilde{\mathcal{I}}, \mathbf{w}, \boldsymbol{\mu}} = \|\boldsymbol{\Omega}_{\tilde{\mathcal{I}}} \mathbf{c}\|_{\text{ALC}^*}^{\tilde{\mathcal{I}}, \mathbf{w}, \boldsymbol{\mu}}. \quad (5)$$

Since the extending operator $\boldsymbol{\Omega}_{\tilde{\mathcal{I}}}$ makes the local patches non-overlapping, the proximity operator of the augmented LCNN can be decoupled with the proximity operator of the weighted NN $\text{prox}_{\gamma \|\cdot\|_{*, \mathbf{w}}}$ for each patch \mathbf{M}_k , which can be computed by the weighted singular value thresholding:

$$\begin{aligned} \text{prox}_{\gamma \mu_k \|\cdot\|_{*, \mathbf{w}}}(\mathbf{M}_k) &= \mathbf{U}_k \Sigma_{\gamma \mu_k \mathbf{w}} \mathbf{V}_k^\top, \\ \Sigma_{\gamma \mu_k \mathbf{w}} &= \text{diag}(\{\sigma_1(\mathbf{X}) - \gamma \mu_k w_1\}_+, \dots, \{\sigma_r(\mathbf{X}) - \gamma \mu_k w_r\}_+), \end{aligned} \quad (6)$$

where \mathbf{U}_k and \mathbf{V}_k are orthogonal matrices obtained via singular value decomposition of \mathbf{M}_k and $\{a\}_+ := \max\{a, 0\}$.

2.2. Primal-Dual Splitting Algorithm

We briefly review a primal-dual splitting algorithm (PDS) [20–22] as a solver of a convex optimization problem used in the experiments in Section 4. Consider the following convex optimization problem to find $\mathbf{x}^* \in \arg \min_{\mathbf{x} \in \mathbb{R}^q} g(\mathbf{x}) + h(\mathbf{L}\mathbf{x})$, where $g \in \Gamma_0(\mathbb{R}^q)$, $h \in \Gamma_0(\mathbb{R}^p)$, and $\mathbf{L} \in \mathbb{R}^{p \times q}$. Then the PDS for solving the problem is given as follows:

$$\begin{cases} \mathbf{x}^{(n+1)} := \text{prox}_{\gamma_1 g}[\mathbf{x}^{(n)} - \gamma_1 \mathbf{L}^\top \mathbf{z}^{(n)}], \\ \mathbf{z}^{(n+1)} := \text{prox}_{\gamma_2 h^*}[\mathbf{z}^{(n)} + \gamma_2 \mathbf{L}(2\mathbf{x}^{(n+1)} - \mathbf{x}^{(n)})], \end{cases} \quad (7)$$

where h^* is the conjugate function³ [24] of h .

3. COLOR AFFINE SUBSPACE PURSUIT

3.1. Problem on LCNN

Before presenting the proposed method, we discuss the problem on the LCNN in this section. Minimizing the cost function with the LCNN can be regarded as shrinking a color distribution of a local patch toward a low dimensional subspace. Thus, the LCNN can efficiently recover patches when the true color distribution (the red-circle samples) is lying around a line that cross the origin as shown in Fig. 3(a), whereas it cannot in the following two cases.

- *Affine subspace:* Even if a local patch forms a line or a plane, it does not necessarily cross the origin. Since image recovery with a LCNN regularization tries to make a color distribution cross the origin, the estimated distribution would differ from the true one when the latent distribution is affine. For example, let us assume the red-circle samples around the line ℓ_1 in Fig. 3(b) are true samples. In this case, the latent samples are wrongly estimated by the (blue-circle) samples around the line ℓ_2 in Fig. 3(b).

³For $\forall f \in \Gamma_0(\mathbb{R}^p)$, the conjugate function f^* of f is defined as: $f^*(\boldsymbol{\xi}) = \sup_{\mathbf{x} \in \mathbb{R}^p} \langle \mathbf{x}, \boldsymbol{\xi} \rangle - f(\mathbf{x})$, and the proximity operator of the conjugate function is defined as: $\text{prox}_{\gamma f^*}(\mathbf{x}) = \mathbf{x} - \text{prox}_{\frac{1}{\gamma} f}(\frac{1}{\gamma} \mathbf{x})$.

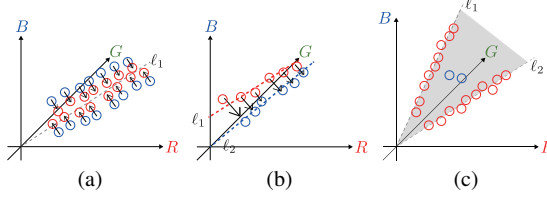


Fig. 3: Color distributions as UoAS: (a) subspace (line), (b) affine subspace (line), (c) union of subspaces (lines)

- *Union of subspaces:* Consider a case that a local patch consists of two lines (the red-circle samples) and two outliers (the blue-circle samples). As shown in Fig. 3(c), to obtain the desired local patch, we should shrink the distribution toward to the lines ℓ_1 and ℓ_2 . However, in this case, a LCNN regularization approximates the latent color distribution toward not lines but a plane (the gray plane in Fig. 3(c)), one cannot distinguish whether the blue-circle samples are outliers or not.

3.2. General Formulation of CASSP

To overcome the problem on LCNN, this section presents a general formulation of CASSP as follows. To characterize a UoAS of a local patch, we model every \mathbf{M}_k as $\mathbf{M}_k \approx \mathbf{W}_k \mathbf{P}_k + \mathbf{D}_k \mathbf{Q}_k$ (see Fig. 4), where $\mathbf{W}_k \in \mathbb{R}_+^{3 \times N_k^{(W)}}$ and $\mathbf{D}_k \in \mathbb{R}_+^{3 \times N_k^{(D)}}$ represent dictionaries to span lines/planes and compensate offsets, respectively (the numbers of columns $\{N_k^{(W)}\}_k$ and $\{N_k^{(D)}\}_k$ should be determined in advance). It is allowed to choose the dictionaries \mathbf{W}_k and \mathbf{D}_k begin redundant, as long as the coefficient matrices $\mathbf{P}_k \in \mathbb{R}^{N_k^{(W)} \times |\mathcal{I}_k|}$ and the binary matrix $\mathbf{Q}_k \in \{0, 1\}^{N_k^{(D)} \times |\mathcal{I}_k|}$ are sparse and low-rank.

Under the setting, the optimal set of variables \mathbf{X}^* and $\Gamma^* = (\{\mathbf{W}_k^*\}, \{\mathbf{P}_k^*\}, \{\mathbf{D}_k^*\}, \{\mathbf{Q}_k^*\})$ promoting the UoAS property should satisfy the following equation:

$$\begin{aligned}
 (\mathbf{X}^*, \Gamma^*) &= \arg \min_{\mathbf{X}, \Gamma} \mathcal{J}(\mathbf{X}, \Gamma), \\
 \mathcal{J}(\mathbf{X}, \Gamma) &:= F_{\mathbf{Y}}(\Phi(\mathbf{X})) + \mathcal{R}_{\text{CASSP}}(\mathbf{X}, \Gamma), \\
 \mathcal{R}_{\text{CASSP}}(\mathbf{X}, \Gamma) &:= \sum_{k=1}^K \lambda_1 \|\mathbf{X}_k - (\mathbf{W}_k \mathbf{P}_k + \mathbf{D}_k \mathbf{Q}_k)\|_F^2 \\
 &\quad + \lambda_2 \|\mathbf{P}_k\|_* + \lambda_3 \|\mathbf{P}_k\|_1 + \lambda_4 \|\mathbf{Q}_k\|_* + \lambda_5 \|\mathbf{Q}_k\|_1 \\
 &\quad + \iota_{\mathbb{R}_+}(\mathbf{W}_k) + \iota_{\mathbb{R}_+}(\mathbf{D}_k) + \iota_{\{0,1\}}(\mathbf{Q}_k), \tag{8}
 \end{aligned}$$

where $F_{\mathbf{Y}}: \mathbb{R}^{3 \times N} \rightarrow \mathbb{R}_+$ is some data fidelity function, and $\iota_{\mathbb{R}_+}$ and $\iota_{\{0,1\}}$ are the indicator function⁴ (we omit the notation for the size of matrices). $\lambda_k \in \mathbb{R}_+$ ($k = 1, \dots, 4$). This cost function is highly ill-posed and non-convex due to the matrix factorization problem.

3.3. CASSP by Centered-cluster-wise LCNN

The optimization of (8) is hard to solve, particularly in finding the optimal matrices \mathbf{W}_k and \mathbf{D}_k . Here, we simplify the cost function for CASSP by using a low-dimensional approximation for each centered cluster. It includes clustering and centering operations to each patch (Fig. 5), which is explained as follows.

⁴The indicator function of a set A ($\iota_A: \mathbb{R}^p \rightarrow \{0, \infty\}$) is defined as $\iota_A(\mathbf{x}) = 0$ ($\mathbf{x} \in A$), $\iota_A(\mathbf{x}) = \infty$ ($\mathbf{x} \notin A$).

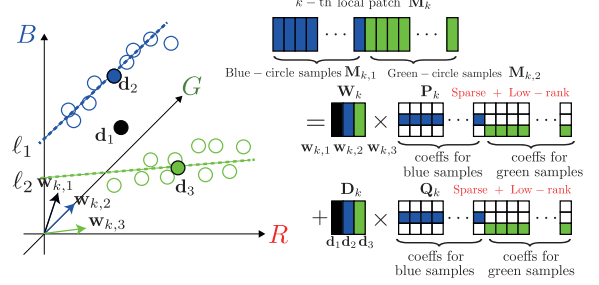


Fig. 4: General CASSP formulation

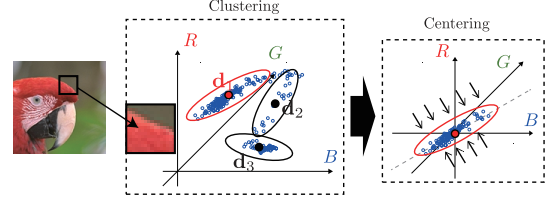


Fig. 5: Centered-cluster-wise LCNN regularization

1. *Pre-recovery:* To apply some clustering technique, a degraded image is firstly recovered by using some regularization, e.g., vectorial total variation [6] in (1).
2. *Clustering:* After the pre-recovery, perform the clustering, e.g., K -means clustering, to each patches, and obtain L_k clusters of the k -th patch. The set of indices of the ℓ -th cluster in the k -th patch is denoted as $\mathcal{I}_{k,\ell}$, the number of its elements as $|\mathcal{I}_{k,\ell}|$, and all the sets of indices is $\tilde{\mathcal{I}}^c := \{\tilde{\mathcal{I}}_k^c\}_{k=1}^K$, where $\tilde{\mathcal{I}}_k^c := \{\mathcal{I}_{k,\ell}\}_{\ell=1}^{L_k}$. Let the R, G, and B channels in the k -th patch of an input image be $\mathbf{M}_{k,\ell} := [\mathbf{c}_{r,k,\ell} \ \mathbf{c}_{g,k,\ell} \ \mathbf{c}_{b,k,\ell}]^\top \in \mathbb{R}^{3 \times |\mathcal{I}_{k,\ell}|}$ the color matrix of the ℓ -th cluster in the k -th patch. an extending operator $\Omega_{\tilde{\mathcal{I}}^c} = [\Omega_{1,1}^\top \ \dots \ \Omega_{K,L_K}^\top]^\top \in \mathbb{R}^{\tilde{N} \times 3N}$, where $\Omega_{k,\ell} \in \mathbb{R}^{|\mathcal{I}_{k,\ell}| \times 3N}$ picks the samples of the ℓ -th cluster in the k -th cluster, i.e., $\Omega_{k,\ell} \mathbf{c} = [\mathbf{c}_{r,k,\ell} \ \mathbf{c}_{g,k,\ell} \ \mathbf{c}_{b,k,\ell}]^\top$. $\mathbf{u}_{k,\ell} = [u_{r,k,\ell} \ u_{g,k,\ell} \ u_{b,k,\ell}]^\top \in \mathbb{R}_+^3$ denotes the center of each cluster.
3. *Centered-cluster-wise LCNN:* To make the optimization problem tractable, we modify LCNN for CASSP. Let $\mathbf{m}_{\tilde{\mathcal{I}}^c} \in \mathbb{R}^{3\tilde{N}}$ be all the centers corrected from all the cluster as

$$\begin{aligned}
 \mathbf{m}_{\tilde{\mathcal{I}}^c} &:= [\mathbf{m}_{1,1}^\top \ \dots \ \mathbf{m}_{1,L_1}^\top \ \dots \ \mathbf{m}_{K,L_K}^\top]^\top \in \mathbb{R}^{3\tilde{N}} \\
 \mathbf{m}_{k,\ell} &:= [u_{r,k,\ell} \mathbf{1}^\top \ u_{g,k,\ell} \mathbf{1}^\top \ u_{b,k,\ell} \mathbf{1}^\top]^\top \in \mathbb{R}^{3|\mathcal{I}_{k,\ell}|} \tag{9}
 \end{aligned}$$

Now, we define the centered-cluster-wise LCNN (ccLCNN) as

$$\begin{aligned}
 \|\mathbf{c}\|_{\text{ccLC}}^{\tilde{\mathcal{I}}^c, \mathbf{w}, \boldsymbol{\mu}^c} &:= \|\mathbf{c} - \mathbf{m}_{\tilde{\mathcal{I}}^c}\|_{\text{LC}}^{\tilde{\mathcal{I}}^c, \mathbf{w}, \boldsymbol{\mu}^c} = \|\Omega_{\tilde{\mathcal{I}}^c} \mathbf{c} - \mathbf{m}_{\tilde{\mathcal{I}}^c}\|_{\text{ccALC}}^{\tilde{\mathcal{I}}^c, \mathbf{w}, \boldsymbol{\mu}^c} \\
 \|\mathbf{c}\|_{\text{ccALC}}^{\tilde{\mathcal{I}}^c, \mathbf{w}, \boldsymbol{\mu}^c} &:= \sum_{k=1}^K \sum_{\ell=1}^{L_k} \mu_{k,\ell} \|\mathbf{M}_{k,\ell}\|_{*, \mathbf{w}}, \tag{10}
 \end{aligned}$$

where $\boldsymbol{\mu}^c := [\mu_{1,1} \ \dots \ \mu_{K,L_K}]^\top \in \mathbb{R}_+^{\sum_k L_k}$ is the cluster-wise relative strength.

Algorithm 1 Solver for (11)

```

1: set  $n = 0$  and choose  $\mathbf{c}^{(0)}, \mathbf{z}_1^{(0)}, \mathbf{z}_2^{(0)}, \gamma_1, \gamma_2$ .
2: while stop criterion is not satisfied do
3:    $\mathbf{c}^{(n+1)} = \text{prox}_{\gamma_1 \iota_{[0,1]}}(\mathbf{c}^{(n)} - \gamma_1(\Phi^\top \mathbf{z}_1^{(n)} + \Omega_{\bar{z}^c}^\top \mathbf{z}_2^{(n)} + \mathbf{D}^\top \mathbf{z}_3^{(n)}))$ 
4:    $\hat{\mathbf{t}}_1^{(n)} = \mathbf{z}_1^{(n)} + \gamma_2 \Phi(2\mathbf{c}^{(n+1)} - \mathbf{c}^{(n)})$ ,
      $\hat{\mathbf{t}}_2^{(n)} = \mathbf{z}_2^{(n)} + \gamma_2 \Omega_{\bar{z}^c}(2\mathbf{c}^{(n+1)} - \mathbf{c}^{(n)})$ ,
      $\hat{\mathbf{t}}_3^{(n)} = \mathbf{z}_3^{(n)} + \gamma_2 \mathbf{D}(2\mathbf{c}^{(n+1)} - \mathbf{c}^{(n)})$ .
5:    $\hat{\mathbf{t}}_1^{(n)} = \text{prox}_{\frac{1}{\gamma_2} \iota_{\mathcal{B}(\mathbf{v}, \epsilon)}}(\frac{1}{\gamma_2} \hat{\mathbf{t}}_1^{(n)})$ ,
      $\hat{\mathbf{t}}_2^{(n)} = \text{prox}_{\frac{1}{\gamma_2} \|\cdot\|_{\text{ccALC}}^c}(\frac{1}{\gamma_2} \hat{\mathbf{t}}_2^{(n)})$ ,
      $\hat{\mathbf{t}}_3^{(n)} = \text{prox}_{\frac{1}{\gamma_2} \|\cdot\|_{1,2}}(\frac{1}{\gamma_2} \hat{\mathbf{t}}_3^{(n)})$ .
6:    $\mathbf{z}_k^{(n+1)} = \hat{\mathbf{t}}_k^{(n)} - \gamma_2 \hat{\mathbf{t}}_k^{(n)}$  ( $k = 1, 2, 3$ ).
7:    $n = n + 1$ .
8: end while
9: Output  $\mathbf{c}^{(n)}$ .

```

Let us discuss the relationship between $\mathcal{R}_{\text{CASSP}}(\mathbf{X}, \Gamma)$ in (8) and $\|\mathbf{c}\|_{\text{ccLC}}$ in (10). Because the clustering gives us the heuristic solution of $(\hat{\mathbf{D}}_k, \hat{\mathbf{Q}}_k)$ in (8), we denote it as $(\hat{\mathbf{D}}_k, \hat{\mathbf{Q}}_k)$, $\mathcal{R}_{\text{CASSP}}(\mathbf{X}, \Gamma)$ can be reduced as:

$$\begin{aligned} \tilde{\mathcal{R}}_{\text{CASSP}}(\mathbf{X}, \{\mathbf{W}_k\}, \{\mathbf{P}_k\}) &:= \sum_{k=1}^K \lambda_1 \|\bar{\mathbf{X}}_k - \mathbf{W}_k \mathbf{P}_k\|_F^2 \\ &+ \lambda_2 \|\mathbf{P}_k\|_* + \lambda_3 \|\mathbf{P}_k\|_1 + \iota_{\mathbb{R}_+}(\mathbf{W}_k), \quad (\bar{\mathbf{X}}_k := \mathbf{X}_k - \hat{\mathbf{D}}_k \hat{\mathbf{Q}}_k). \end{aligned}$$

The above sparse and low-rank representation acts as a low-dimensional approximation for each centered cluster, and thus the ccLCNN can be regarded as a simple substitution of (8).

4. EXPERIMENTAL RESULTS

We evaluated the performance of the proposed ccLCNN-based CASSP with VTV (VTV + ccLCNN) in compressed sensing reconstructions and compared with the VTV, and the VTV + LCNN [15]. As test images, we use *Parrots* and the 300 images of the *Berkeley Segmentation Database* (BSDS300) [25]. Fig. 6 shows the original images $\mathbf{c} \in \mathbb{R}^{256^2}$ (left) and the observed images (right). Each incomplete observation $\mathbf{v} = \Phi \mathbf{c} + \mathbf{n}$ ($\Phi := \mathbf{S} \tilde{\Phi}$) is obtained by the Noiselet transform [26] $\tilde{\Phi}$ followed by random downsampling $\mathbf{S} \in \mathbb{R}^{M \times 3N}$ ($M = 0.2 \times 3N$) in the presence of an additive white Gaussian noise \mathbf{n} with standard derivation 0.1.

The cost function of VTV + ccLCNN for compressed sensing reconstructions is formulated as follows.

$$\begin{aligned} \mathbf{c}^* &= \arg \min_{\mathbf{c} \in \mathbb{R}^{3N}} F_{\mathbf{v}}(\Phi \mathbf{c}) + \lambda_1 \|\Omega_{\bar{z}^c} \mathbf{c} - \mathbf{m}_{\bar{z}^c}\|_{\text{ccALC}}^c \\ &+ \lambda_2 \|\mathbf{D} \mathbf{c}\|_{1,2} + \iota_{[0,1]}(\mathbf{c}), \end{aligned} \quad (11)$$

where we used $F_{\mathbf{v}}$ as the indicator function of the ℓ_2 -norm ball $\iota_{\mathcal{B}(\mathbf{v}, \epsilon)}(\mathcal{B}(\mathbf{v}, \epsilon) := \{\mathbf{x} \in \mathbb{R}^M \mid \|\mathbf{x} - \mathbf{v}\|_2 \leq \epsilon\}, \epsilon = \|\Phi \mathbf{c} - \mathbf{v}\|_2)$, $\lambda_1 = 2, \lambda_2 = 1$. For the LCNN and the ccLCNN, the patches size is 16×16 , the patches is horizontally, vertically, and diagonally overlapping 8 pixels, and $\mathbf{w} = [0.001, 1, 1]^\top$. In the ccLCNN, K -means clustering with the number of cluster $L_k = 3$ ($\forall k$) is used. For the LCNN $\mu_k = 1$ ($\forall k$), whereas $\mu_{k,\ell} = 1$ ($|\mathcal{I}_{k,\ell}| > 0.2|\mathcal{I}_k|$), $\mu_{k,\ell} = 0.3$ ($0.1|\mathcal{I}_k| < |\mathcal{I}_{k,\ell}| \leq 0.2|\mathcal{I}_k|$), $\mu_{k,\ell} = 0.18$ ($|\mathcal{I}_{k,\ell}| \leq 0.1|\mathcal{I}_k|$) for the ccLCNN. \mathbf{D} is the vertical and horizontal differential matrix defined as $\mathbf{D} = \mathbf{I}_3 \otimes \mathbf{D}_0 \in \mathbb{R}^{6N \times 3N}$, where $\mathbf{D}_0 = [\mathbf{D}_v^\top \ \mathbf{D}_h^\top]^\top$. $\|\cdot\|_{1,2}$ is the mixed $\ell_{1,2}$ norm [19]. $C_{[0,1]}$ is the set of vectors whose



Fig. 6: (a)–(e) Original images (256×256) and observed images

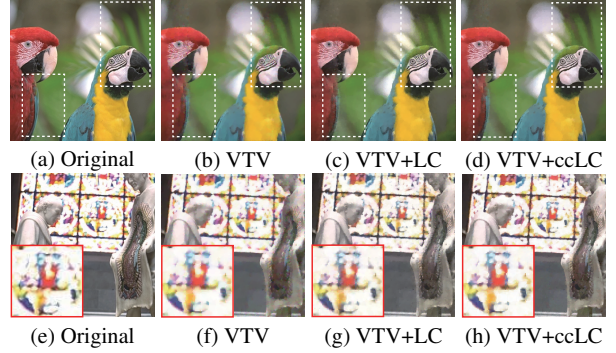


Fig. 7: Resulting images of *Image 1* and *Image 2*

Table 1: Numerical Error (PSNR [dB])

	<i>Image 1</i>	<i>Image 2</i>	<i>Image 3</i>	<i>Image 4</i>	<i>Image 5</i>	Ave.
VTV	30.51	25.55	25.61	25.51	27.50	28.00
VTV+LC	30.76	26.43	26.62	26.54	28.15	29.37
VTV+ccLC	32.08	27.06	27.04	27.53	28.78	29.74

entries are within $[0, 1]$. In order to solve (11) by PDS, the functions g and h , and the matrix \mathbf{L} in (7) are set as:

$$\begin{aligned} g(\mathbf{c}) &= \iota_{C_{[0,1]}}(\mathbf{c}), \quad \mathbf{z} = [\mathbf{z}_1^\top \ \mathbf{z}_2^\top \ \mathbf{z}_3^\top]^\top = \mathbf{L} \mathbf{c}, \\ h(\mathbf{z}) &= \iota_{\mathcal{B}(\mathbf{v}, \epsilon)}(\mathbf{z}_1) + \lambda_1 \|\mathbf{z}_2 - \mathbf{m}_{\bar{z}^c}\|_{\text{ccALC}}^c + \lambda_2 \|\mathbf{z}_3\|_{1,2}, \\ \mathbf{L} &= [\Phi^\top \quad \Omega_{\bar{z}^c}^\top \quad \mathbf{D}^\top]^\top. \end{aligned} \quad (12)$$

Then, a solver of (11) can be described in Algorithm 1 (see [15] for the detail of each proximal operator). The stopping criteria is $\|\mathbf{c}^{(n)} - \mathbf{c}^{(n-1)}\|_2 < 0.01$.

As shown in Table 1 (“Ave.” means the average of all the resulting PSNRs from the BSDS300), the VTV + ccLCNN could reduce the reconstruction error, compared with the VTV and the VTV + LCNN. Moreover, as shown in Fig. 7, color smearing and fading artifacts are reduced in the resulting images of the VTV + ccLCNN, compared with that of the VTV and the VTV + LCNN.

5. CONCLUDING REMARKS

This paper proposed a CASSP method for color artifact removal. Local patches in natural color images often do not satisfy the color line property but the color UoAS property. LCNN cannot efficiently estimate the latent image. In this work, we introduce the CASSP approach to promote the color UoAS property. First the UoAS was characterized by sparse and low-rank representation by two dictionaries. The cost function, however, involves a matrix factorization problem that make it hard to solve. Thus, we simplify the cost function by using ccLCNN evaluating LCNN to each centered cluster after image pre-recovery clustering. Experimental results showed that CASSP recovered latent images more robustly than the conventional LCNN in both numerical reconstruction error and subjective visual quality.

6. REFERENCES

- [1] P. L. Combettes and J.-C. Pesquet, "A proximal decomposition method for solving convex variational inverse problems," *Inverse Problems*, vol. 24, no. 6, pp. 065014, Nov. 2008.
- [2] T. Goldstein and S. Osher, "The split Bregman method for L1-regularized problems," *SIAM J. Imag. Sci.*, vol. 2, no. 2, pp. 323–343, Apr. 2009.
- [3] N. Pustelnik, C. Chau, and J. Pesquet, "Parallel proximal algorithm for image restoration using hybrid regularization," *IEEE Trans. Image Process.*, vol. 20, no. 9, pp. 2450–2462, Sep. 2011.
- [4] M. V. Afonso, J. M. B.-Dias, and M. A. T. Figueiredo, "An augmented lagrangian approach to the constrained optimization formulation of imaging inverse problems," *IEEE Trans. Image Process.*, vol. 20, no. 3, pp. 681–695, Mar. 2011.
- [5] L. I. Rudin, S. Osher, and E. Fatemi, "Nonlinear total variation based noise removal algorithms," *Phys. D*, vol. 60, no. 1-4, pp. 259–268, Nov. 1992.
- [6] X. Bresson and Tony F. Chan, "Fast dual minimization of the vectorial total variation norm and applications to color image processing," *Inverse Probl. Imag.*, vol. 2, no. 4, pp. 455–484, Nov. 2008.
- [7] R. H. Chan, Y. Dong, and M. Hintermuller, "An efficient two-phase L^1 -TV method for restoring blurred images with impulse noise," *IEEE Trans. Image Process.*, vol. 19, no. 7, pp. 1731–1739, Jul. 2010.
- [8] I. Bayram and M. E. Kamasak, "Directional total variation," *IEEE Signal Process. Letters*, vol. 19, no. 12, pp. 781–784, Sep. 2012.
- [9] S. Ono and I. Yamada, "Decorrelated vectorial total variation," in *Proc. 2014 IEEE Conference on Computer Vision and Pattern Recognition*, Jun. 2014, pp. 4090–4097.
- [10] K. Bredies, K. Kunisch, and T. Pock, "Total generalized variation," *SIAM J. Imag. Sci.*, vol. 3, no. 3, pp. 492–526, Sep. 2010.
- [11] A. Danielyan, V. Katkovnik, and K. Egiazarian, "BM3D frames and variational image deblurring," *IEEE Trans. Image Process.*, vol. 21, no. 4, pp. 1715–1728, Apr. 2012.
- [12] J. Sulam, B. Ophir, M. Zibulevsky, and M. Elad, "Trainlets: Dictionary learning in high dimensions," *IEEE Trans. Signal Process.*, vol. 64, no. 12, pp. 3180–3193, Jun. 2016.
- [13] G. Chierchia, N. Pustelnik, B. Pesquet-Popescu, and J. C. Pesquet, "A nonlocal structure tensor-based approach for multicomponent image recovery problems," *IEEE Trans. Image Process.*, vol. 23, no. 12, pp. 5531–5544, Dec. 2014.
- [14] S. Lefkimiatis and S. Osher, "Nonlocal structure tensor functionals for image regularization," *IEEE Trans. Image Process.*, vol. 1, no. 1, pp. 16–29, Mar. 2015.
- [15] S. Ono, K. Shirai, and M. Okuda, "Vectorial total variation based on arranged structure tensor for multichannel image restoration," in *Proc. IEEE Int. Conf. Acoust, Speech, Signal Process. (ICASSP)*, Mar. 2016, pp. 4528–4532.
- [16] J. Mairal, M. Elad, and G. Sapiro, "Sparse representation for color image restoration," *IEEE Trans. Image Process.*, vol. 17, no. 1, pp. 53–69, Jan. 2008.
- [17] B. Goldluecke, E. Strekalovskiy, and D. Cremers, "The natural vectorial total variation which arises from geometric measure theory," *SIAM J. Imag. Sci.*, vol. 5, no. 2, pp. 537–563, Apr. 2012.
- [18] S. Ono and I. Yamada, "A convex regularizer for reducing color artifact in color image recovery," in *Proc. IEEE Conf. Comput. Vis. Pattern Recognit. (CVPR)*, Jun. 2013, pp. 1775–1781.
- [19] S. Ono and I. Yamada, "Color-line regularization for color artifact removal," *IEEE Trans. Comput. Imag.*, vol. 2, no. 3, pp. 204–217, Sep. 2016.
- [20] A. Chambolle and T. Pock, "A first-order primal-dual algorithm for convex problems with applications to imaging," *J. Math. Imag. Vis.*, vol. 40, no. 1, pp. 120–145, Dec. 2010.
- [21] L. Condat, "A primal–dual splitting method for convex optimization involving lipschitzian, proximable and linear composite terms," *Journal of Optimization Theory and Applications*, vol. 158, no. 2, pp. 460–479, Aug. 2013.
- [22] B. C. Vu, "A splitting algorithm for dual monotone inclusions involving cocoercive operators," *Adv. Comput. Math.*, vol. 38, no. 3, pp. 667–681, Nov. 2011.
- [23] N. Komodakis and J. C. Pesquet, "Playing with duality: An overview of recent primal-dual approaches for solving large-scale optimization problems," *IEEE Signal Process. Mag.*, vol. 32, no. 6, pp. 31–54, Nov. 2015.
- [24] H. H. Bauschke and P. L. Combettes, *Convex Analysis and Monotone Operator Theory in Hilbert Spaces*, New York, NY, USA: Springer-Verlag, 2011.
- [25] D. Martin, C. Fowlkes, D. Tal, and J. Malik, "A database of human segmented natural images and its application to evaluating segmentation algorithms and measuring ecological statistics," in *Proc. IEEE Int. Conf. Comput. Vis. (ICCV)*, Jul. 2001, vol. 2, pp. 416–423.
- [26] R. Coifman, F. Geshwind, and Y. Meyer, "Noiselets," *Applied and Computational Harmonic Analysis*, vol. 10, no. 1, pp. 27–44, 2001.